Spectroscopic properties of oxygen vacancies in LaAlO₃

Oliver A. Dicks[*] and Alexander L. Shluger

Department of Physics and Astronomy, University College London, Gower Street, London WC1E 6BT, United Kingdom

Peter V. Sushko

Physical & Computational Sciences Directorate, Pacific Northwest National Laboratory, Richland, Washington 99352, United States

Peter B. Littlewood

Argonne National Laboratory, 9700 S. Cass Avenue, Lemont, Illinois 60439, United States

Oxygen vacancies in LaAlO₃ (LAO) play an important role in the formation of the two-dimensional electron gas observed at the LaAlO₃/SrTiO₃ interface and affect the performance of MOSFETs using LAO as a gate dielectric. However, their spectroscopic properties are still poorly understood, which hampers their experimental identification. Here we predict the absorption spectra and ESR parameters of oxygen vacancies in LAO using periodic and embedded cluster methods and density functional theory (DFT). The structure, charge distribution, and spectroscopic properties of the neutral (V_O^0) and charged (V_O^+ and V_O^{2+}) oxygen vacancies in cubic and rhombohedral LaAlO₃ are investigated. The highest intensity optical transitions [calculated using time-dependent DFT (TDDFT)], from the oxygen vacancy states to the conduction-band states have onsets at 3.5 and 4.2 eV for V_O^0 and 3.6 eV for V_O^+ in rhombohedral LAO and 3.3 and 4.0 eV for V_O^0 and 3.4 eV for V_O^+ in cubic LAO, respectively. Also reported are the isotropic g value (2.004026) and hyperfine coupling constants of V_O^+, which are compared to the experimental data obtained using electron spin resonance (ESR) spectroscopy, and accurately predict both the position and the width (3 mT) of its ESR signature. These results may further facilitate the experimental identification of oxygen vacancies in LAO and help to establish their role at the LAO/STO interfaces and in nanodevices using LAO.

I. INTRODUCTION

Understanding the structure and properties of point defects in complex oxides and mechanisms of controlling their properties facilitates the development of new functional materials with tuneable performance characteristics. Not surprisingly, this is an area of active experimental, theoretical and computational research [1,2].

LaAlO₃ (LAO), is of interest because its relatively large band gap, reported to be between 5.6 and 6.3 eV [3,4], may allow for the oxygen vacancies in several charge states, thus, resulting in a range of optical absorption energies. LAO is also used as a substrate for other metal oxide thin films and has potential application as a gate dielectric in complementary metal-oxide-semiconductor (CMOS) devices [5,6]. Defects in the gate oxide can act as carrier traps and scattering centres and understanding their properties is key to controlling the quality and functionality of these oxides.

The bulk of cubic LAO can be represented as a sequence of positively and negatively charged atomic planes [LaO]⁺ and [AlO₂]⁻, respectively, oriented perpendicularly to the [001] direction. Such polar structure makes LAO thin films a functional building block which, for example, can be used as source of electric field in perovskite heterostructures. A well-known example utilizing this principle is the LaAlO₃/SrTiO₃ (LAO/STO) interface, in which mismatch of the SrTiO₃ and LaAlO₃ polarities results in the formation of two-dimensional electron gas (2DEG) [7]. This phenomenon was originally

attributed to the polar catastrophe [1,8–11] and defects in the STO [12]. Recent studies highlighted the importance of the cation intermixing [13–15], the LAO stoichiometry [16,17] and oxygen vacancies (V_O) in LAO on the electronic properties [18] of the LAO/STO interfaces. Zunger *et al.* [19] suggest that the conductivity is a result of an interplay between surface oxygen vacancies in LAO and cation antisite defects at the interface, while Huijben *et al.* [20] have shown that a layer of SrCuO₂ at the LAO/STO interface suppresses oxygen defects and increases mobility, allowing control over the electronic properties through defect engineering.

LAO has a perovskite lattice structure. It has a rhombohedral ($R\bar{3}c$) structure at room temperature and undergoes a phase transition to a cubic ($Pm\bar{3}m$) structure at ~ 839 K [21,22]. When grown as a thin supported film, rhombohedral LAO is considered to be pseudocubic [23], with oxygen octahedra rotations in an antiphase order. However, in order to achieve a crystalline, as opposed to amorphous, thin film of LAO, annealing at or above 650 °C is required [22,24,25], which is above the rhombohedral to cubic phase transition temperature. It is understood that details of the LAO structure in thin films and multi-layered heterostructures depend on the lattice and polarity mismatch with the substrate and over-layers.

Experimentally, defects in LAO have been probed using photoluminescence (PL) spectroscopy [26,27] and electron spin resonance (ESR) [28,29]. Kawabe *et al.* [26] excited LAO using a 266- nm pulsed laser and observed slow emission at 2.5 eV (490 nm), which they attributed to oxygen vacancies, due to its sensitivity to the oxygen content. In order to more directly probe defect states in the band gap, Chen *et al.*

---

[*]Corresponding author: oliver.dicks.11@ucl.ac.uk

[27] used sub-band-gap excitation (400 nm) PL spectroscopy. They observed sharp emissions at 1.7 and 1.8 eV and a broad emission band at 1.9–2.2 eV. They suggested that the excitations occur from the O $2p$ valence band to states within the gap, and therefore PL is a result of decay from these levels. In the ESR experiments [28,29], a broad signal is attributed to an F^+ like center, which was cautiously associated with a charged oxygen vacancy (V_O^+). Accurate modeling of the neutral and charged oxygen vacancies in LAO will allow more confident assignment of these transitions and will help to predict their behavior in the presence of external stimuli.

Previous computational studies of defects in LAO include calculations of oxygen vacancies in cubic LAO using density functional theory (DFT) and generalized gradient approximation (GGA) functionals [30,31] as well as more recent studies [32–34] performed using the hybrid density functional HSE06 [35]. Due to the well-known deficiencies of GGA density functionals, the band gap obtained in these studies (3.1–3.8 eV) was underestimated, while the hybrid density functional predicted the band gaps in the interval of 5.0–5.9 eV, which is in a good agreement with experiment, though the higher value of 5.9 eV was only achieved through increasing the percentage of exact exchange to 32% [34].

The predicted positions of the occupied vacancy levels vary significantly, depending on the types of the density functional and the size of the simulation supercell. Choi *et al.* [34] found the V_O^0 one-electron energy level to lie 3.27 eV above the VBM, with the occupied V_O^+ level lying lower in energy at 2.96 eV, whereas El-Mellouhi *et al.* [33] predicted the neutral level to be at 2.8 eV with the V_O^+ level lying higher at 3.56 eV above the VBM. Thus there is lack of consensus not only on the positions of the energy levels of the neutral and charged oxygen vacancies with respect to the valence-band maximum (VBM) and conduction-band minimum (CBM) but also on the ordering of these levels.

In this work, the electronic and geometric structure of the neutral and charged oxygen vacancies in the band gap of LAO were calculated using DFT with hybrid functionals and periodic and embedded cluster methods. The time-dependent density functional theory [36,37] (TDDFT) and an embedded cluster approach are used to calculate the excitation energies for both neutral and charged oxygen vacancies, improving on the one-electron energy levels previously calculated. The ESR parameters are also calculated and compared to the available experimental data. To compare our results to the previous computational studies and evaluate the difference between bulk and supported thin-film LAO, the calculations are performed for both rhombohedral and cubic lattice structures.

II. METHODOLOGY

The periodic and embedded cluster methods used to study the electronic and geometric structures of the neutral and charged oxygen vacancies in the bulk of LAO are described below.

A. Embedded cluster calculations

In the embedded cluster method, a "region of interest" treated quantum mechanically (QM region in Fig. 1) is
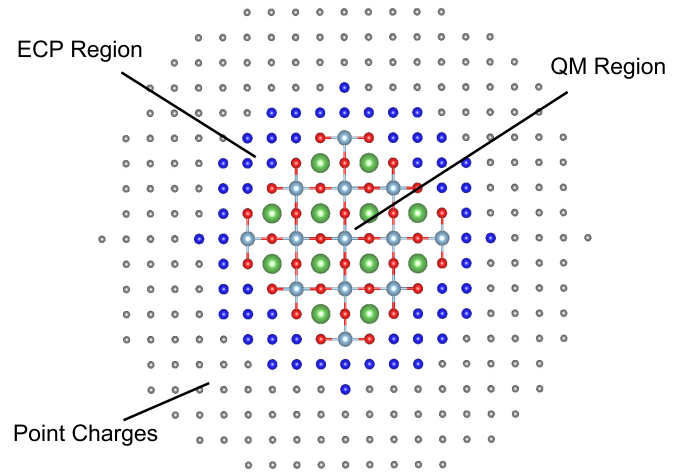

FIG. 1. Schematic setup for the embedded cluster calculations. The central region is treated quantum mechanically (QM region shown is a cross section of that used in the calculations). It is embedded into the long-range electrostatic potential of the infinite lattice, represented by a finite number of point charges, and the short-range potential modeled using large radius effective core pseudopotentials (ECPs) at the interface between the QM region and the point charges.

embedded into the electrostatic potential produced by the rest of the lattice. A detailed description of this method, including the description of long-range defect-induced lattice polarization is given in Ref. [38].

Here, the bulk LAO was represented using a spherical nanoscale cluster constructed of the crystal unit cells. Each unit cell was modified so as their multipole moments M are zero up to $M = 4$ (hexadecapole), as described elsewhere [39,40]. This approach guarantees that the electrostatic potential inside a finite nanoscale cluster converges absolutely to the Ewald potential in the infinite crystalline lattice as the size of the cluster increases. In our case, the nanocluster radius is 30 Å, which provides the convergence of the electrostatic potential to within 0.02 V of the Ewald potential inside the sphere of 11 Å in the central part of the nanocluster.

The QM region at the center of the nanocluster contains 197 atoms and has the chemical composition La$_{32}$Al$_{33}$O$_{132}$. The QM region is chosen so that it is symmetrical, as close to stoichiometry as possible while still fully coordinating all lattice atoms in the first and second atomic shells near the vacancy site and large enough to minimize wave-function confinement, which noticeably affects the value of the band gap for small QM regions. In order to confine the electron density to the QM region, all cations also have to be capped with oxygens.

The QM region is surrounded by the shell of the interface atoms represented by large core effective pseudopotentials (ECP) in order to confine the electron density within the QM region (see Fig. 1). The width of this shell is ~ 10 Å, which allows one to use diffuse basis set functions for the atoms of the QM cluster and, yet, avoid spurious effects associated with electrons transfer outside the QM region. All other atoms of the nanocluster are represented by point charges.

All oxygens species in the QM region are treated using the full electron 6–311G basis set [41] as are the Al [42]. The La inside the QM region were described by a contracted version of the LANL08 basis set [43] and the LANL2DZ ECP [44] from the EMSL basis set exchange [45].

Outside the QM region, the La and Al ions were described by ECPs, as they both have a formal charge of +3 $|e|$ and, thus, require ECPs in order to prevent the artificial polarization of the QM region electron density. The Al ions are modeled using the LANL2 ECP [44], and the La ions are modeled using the LANL2DZ ECP [44] from the ESML basis set exchange[45].

The geometrical structure of the material in the electronic ground state was determined by minimizing the total energy of the system with respect to the coordinates of atoms out to 5.72 Å from the central Al in the cluster. This allows all nearest neighbor La, Al and O to the vacancy site to relax. TDDFT calculations and the Frank-Condon approximation were used to calculated the excitation energies and relative intensities. All calculations were carried out using the GAUSSIAN09 package [46].

For all calculations using the embedded cluster method the HSE06 [47] functional was used, which was shown to accurately predict the band gap and, as such, will allow comparison with previous results. The self-consistent field (SCF) convergence criterion is set to an energy difference of 10^{-7} Hartree. For the geometrical relaxations the convergence criterion is set to a force of 0.0017 Hartree/Bohr on the atoms being relaxed.

B. Periodic calculations

The bulk properties of the cubic and rhombohedral LAO were calculated in the Γ point using the 135 and 270 atoms supercells, respectively, and the CP2K [48] package. We used the PBE0-TC-LRC [49] functional with a cutoff radius of 5.5 Å due to the computational expense of running calculations using HSE06 [47] on the larger rhombohedral system. The form of truncation used means that calculations are faster in CP2K using PBE0-TR-LRC than HSE06 because they are done in real space. However, the energy-level ordering and molecular orbitals agreed well with calculations performed

using the HSE06 functional for the cubic system. CP2K makes use of hybrid Gaussian and plane wave type basis sets. The DZVP-MOLOPT-SR-GTH [50] basis sets were used for both O and Al, along with the Goedecker-Teter-Hutter (GTH) pseudopotentials [51,52]. The converged plane wave energy cutoff was set to 400 Ry and the SCF convergence criteria was set to a maximum energy difference of 10^{-6} Hartree between steps. All calculations were performed at the Γ point. All geometry relaxations were performed using the conjugate gradient optimizer with a maximum force convergence criterion of 0.001 Hartree/Bohr for each atom.

III. RESULTS AND DISCUSSION

A. Ground-state calculations

1. The perfect lattice

Cell optimizations of the perfect lattice for the cubic phase were performed using PBE0-TR-LRC. The calculated lattice parameter of $a = 3.79$ Å agrees well with the experimentally measured lattice parameter of $a = 3.8108$ Å [21]. Due to the computational expense, the experimental lattice parameters were used for the larger rhombohedral supercell.

The one-electron band gaps calculated using both the periodic and embedded cluster methods are shown in Figs. 2 and 3. The optical band gap of rhombohedral LAO is 5.6 eV, as measured by Lim *et al.* [3] using UV spectroscopic ellipsometry. The reported absorption spectra show a sharp absorption edge, as expected for a direct band gap material. No sharp peaks associated with d-state to d-state transitions were observed, suggesting that the VBM is composed of O $2p$ orbitals. The band gaps of amorphous thin films of LAO grown by molecular beam deposition (MBD) have been measured by Cicerella *et al.* [4] to be 5.84–6.33 eV depending on film thickness. It is possible that these films have a pseudocubic crystalline structure as they were annealed at 900 °C, i.e., well above the 650 °C, which other groups have determined is necessary for amorphous films to become crystalline [22,24,25].

The calculated one-electron band gaps of rhombohedral LAO (5.74 and 5.98 eV for the periodic and embedded cluster
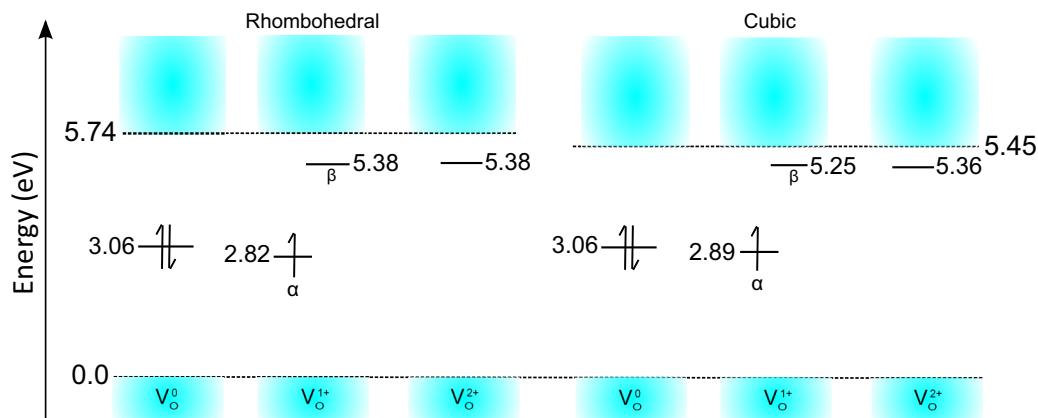

FIG. 2. The one-electron energy levels for the neutral and charged oxygen vacancies from the periodic calculations of the rhombohedral and cubic phases. The numbers show the positions of the Kohn-Sham energy levels calculated with respect to the top of the valence band for each system. The band gaps shown in larger font are from the defect free calculations. The α and β symbols refer to the electron spin state of the V_O^+, in this diagram the α state in the gap is occupied while the β is unoccupied.
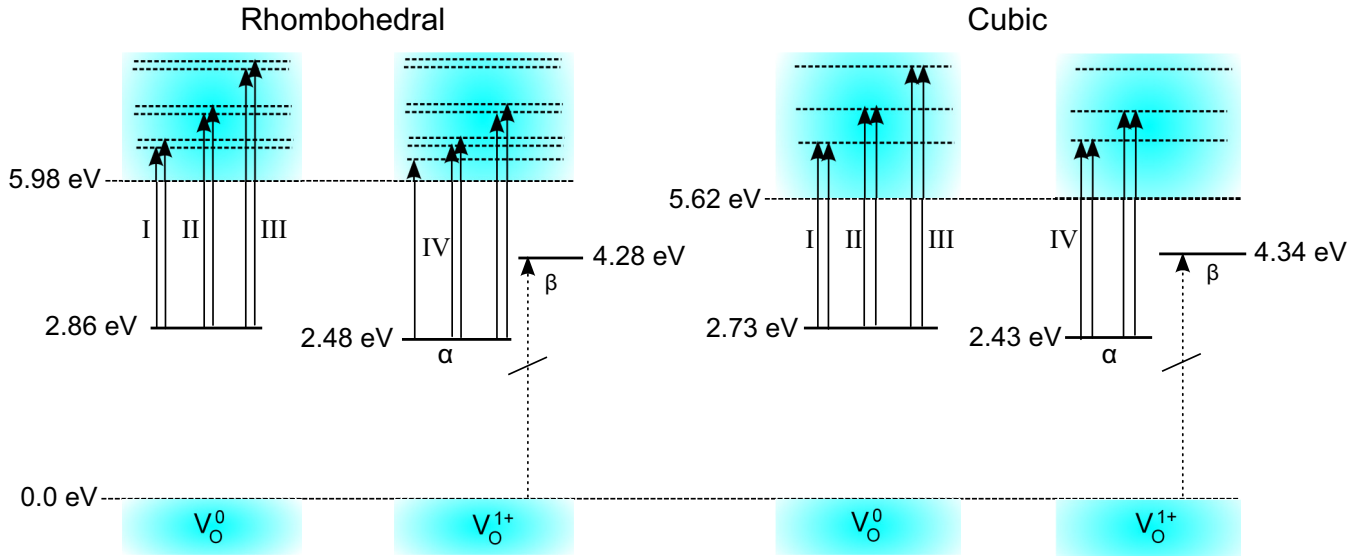
FIG. 3. The one-electron energy levels and band gaps from the embedded cluster calculations for the cubic and rhombohedral LAO phases (energies not to scale). Arrows show the types of the optical transitions and the character of the states involved in these transitions. The α and β symbols refer to the electron spin state, in this diagram the α state in the gap is occupied, while the β is unoccupied.

calculations, respectively) are both within the range set by the experimental measurements, and only differ by ~ 0.2 eV showing good agreement between these methodologies. As can be seen in Fig. 4, the main orbital contributions to the VBM and CBM are consistent with experiment [3] with the VBM being constructed from O $2p$ orbitals and the CBM being made of La d orbitals. This was found to be the case for both the periodic and embedded cluster calculations.

The band gap of the cubic LAO (5.45 and 5.62 eV for the periodic and embedded cluster calculations, respectively) is smaller than that of the rhombohedral LAO by ~ 0.3 eV, consistent across both the periodic and embedded cluster calculations. The band gap values are close to those of Choi
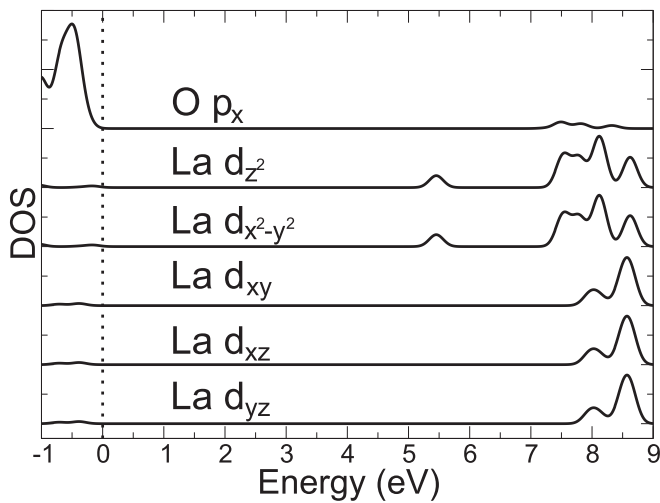

FIG. 4. The projected densities of states (PDOS) for the defect free bulk sytem of cubic LAO calculated using the periodic method. The character of the VBM is dominated by the O p and the CBM by the La d orbitals. The energies are with respect to the top of the valence band. The black dashed line indicates the Fermi energy position at the top of the valence band.

et al. [34], who predict 5.92 eV for the rhombohedral and 5.30 eV for the cubic phases. Choi *et al.* also show a similar band gap shift relationship between cubic and rhombohedral structures to the results given in this paper.

2. The oxygen vacancy

According to our calculations, the two electrons associated with a neutral oxygen vacancy in LAO, either cubic or rhombohedral, localize on the vacancy site [see Fig. 5(a)]. The corresponding doubly occupied energy level is approximately in the middle of the band gap. This localization character suggests that the vacancy can be classified as an F center. Similar charge localization is seen in other nonreduceable metal oxides including Al_2O_3 and other perovskites [53]. The largest orbital contributions to the vacancy state are from the nearest-neighbor Al p orbitals, the lobes of which point towards the vacancy, with the second largest contribution being from the nearest-neighbor La d orbitals.

The formation energies of the neutral and charged oxygen vacancies were calculated using the method outlined by Lany and Zunger [54]. The formation energy is given by the formula

$$\Delta H_{D,q} = [E_{D,q} - E_{bulk}] + \sum_{\alpha} n_{\alpha}\mu_{\alpha} + q(E_V + \Delta E_F),$$

where $\Delta H_{D,q}$ is the formation energy of a defect D with charge q, $E_{D,q}$ and E_{bulk} are the total energy of the system with and without the defect, respectively, n_{α} are the numbers of species of each type (La, Al, and O) removed from the bulk cell, and μ_{α} are their respective chemical potentials. E_V is the difference between the energies of the bulk neutral system and the bulk system with a charge q and ΔE_F is the difference between the Fermi level (electron chemical potential) and the VBM.

The formation energies were calculated using both periodic and embedded cluster methods. The chemical potential of oxygen was taken as half of the total energy of the O_2 molecule in the triplet state. For the embedded cluster calculations, the
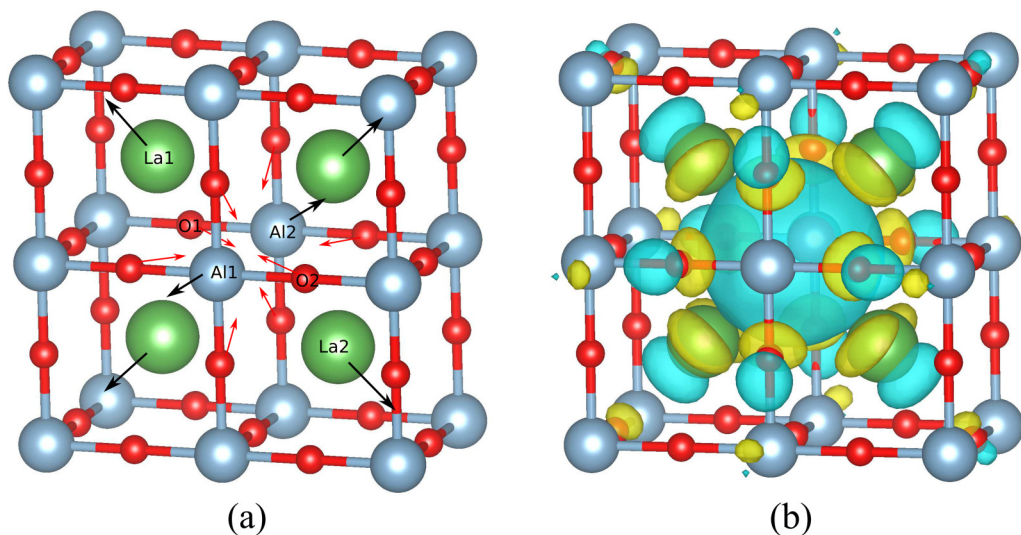
FIG. 5. (a) The directions of the ion displacements induced by a positively charged vacancy are shown by the arrows. The La1–La2, Al1–Al2, and O1–O2 distances are given as La–La, Al–Al, and O–O distances, respectively, in Table I. (b) The one-electron state of the neutral oxygen vacancy calculated using the periodic method in cubic LAO. Characteristically of a *F*-center vacancy type, electrons are trapped on the vacancy site.

total energy of an isolated O_2 molecule was calculated using GAUSSIAN09 and the same oxygen basis sets, functional, and convergence criteria as for the LAO cluster. In the periodic method calculations, the energy of the molecule was calculated using an orthorhombic $20 \times 22 \times 25$ Å^3 cell, with the same calculations parameters as those used for the bulk LAO. Due to the large size of the cell and the high dielectric constant of LAO an energy correction due to the interaction between periodically translated charged defects is negligible (<0.01 eV).

For rhombohedral LAO, the V_O^0 formation energy was calculated to be 6.5 eV from the periodic calculations and 7.2 eV from the cluster calculations. The difference of 0.7 eV between the formation energies calculated by the two methods is largely due to the difference in the oxygen chemical potential reference energy. As stated earlier, the oxygen chemical potential is taken as half the energy of an O_2 molecule, which is used to model the typical oxygen environment of LAO during growth. However, the binding energy of the molecule is different in the two methods. If instead, the energy of a single atomic oxygen is taken as the chemical potential, the difference in formation energies between the two methods drops to 0.3 eV. The values for the V_O^0 formation energies in rhombohedral LAO presented in this paper are lower than the formation energy of 8.3 eV reported by Mitra *et al.* [32]. The referenced calculations were performed using the HSE06 functional, however, only an 80-atom supercell was used, which would limit the relaxation around the defect site compared to the larger cell of 270 atoms used in this work. In the same paper using the PBE functional, it is shown that supercell size has a large impact on formation energies, even for neutral vacancies. This suggests the formation energies calculated for the larger cells are more reliable. The formation energies of the oxygen vacancies as a function of Fermi energy are shown in Fig. 6. (It must be clarified that this picture is only valid when the LAO bulk is attached to an idealized Fermi sea of electrons, generally provided by a metal or semiconductor electrode.) Even so, we can see that thermodynamically V_O^0

and V_O^{2+} are the most stable defects, with V_O^{2+} having the lowest formation energy if the Fermi level is near the top of the valence band. If the Fermi level exceeds 3.6 eV above the VBM, V_O^0 has the lowest formation energy.

This is relevant to the LAO/Si transistor devices, where valence-band offsets of 2.86 eV have been measured using x-ray photoelectron spectroscopy [6], suggesting that charged oxygen vacancies will form upon contact with undoped silicon. In turn, if the Si channel is *n*-doped, i.e., the Fermi level is 3.8 eV or more above the LAO VBM, the vacancies can trap electrons, which would affect device operation.

The direction of vacancy-induced atomic displacements (see Fig. 5) are as expected for the ionic system, and the magnitudes of these displacements are in good agreement between the cluster and periodic calculations. The small
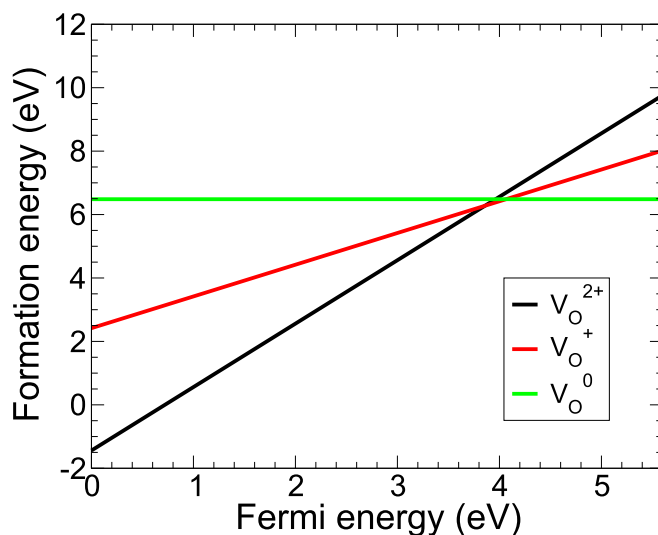

FIG. 6. Formation energies of V_O^0, V_O^+, V_O^{2+} as a functions of Fermi energy above the VBM for the periodic method calculations of rhombohedral LAO.

displacements of ions around the neutral vacancy are consistent with that reported earlier for LAO [34] and is consistent with calculations of similar perovskites such as $SrTiO_3$ [55]. The larger displacements, especially those of Al species, induced by the positively charged vacancies, are consistent with other DFT studies of oxygen vacancies in LAO [34]. This also explains the higher formation energies reported by Mitra *et al.* [32]: in a smaller supercell lattice relaxation is constrained by the periodic boundary conditions and the final energy of the system is correspondingly higher.

Both the periodic and cluster methods (see Figs. 2 and 3) agree on the ordering of the one-electron energy levels, with the V_O^+ level lying below the V_O^0 level and the unoccupied V_O^{2+} level lying closest to the CBM. These results are consistent with those reported by Choi *et al.* [34], but disagree with those published by Mitra *et al.* [32] who calculate the V_O^+ level to lie 1.34 eV above V_O^0. This difference could be attributed to a smaller supercell used in Ref. [32] (an 80-atom supercell) meaning stronger defect-defect interactions for the charged vacancies. In all calculations reported in this paper, the one-electron band gap does not change with respect to the charge of the defect by more than 0.05 eV as a result of large enough cluster and cell sizes to mitigate confinement and defect-defect interactions.

The possibility of a stable V_O^- state existing in LAO was also investigated. The extra electron was not found to localize at the vacancy site but, instead, occupied delocalized states at the bottom of the conduction band. For comparison, V_O^- and V_O^{2-} were shown to exist in HfO_2, which has band gap and dielectric constant similar to those of LAO [56]. These vacancy charge states are stabilized by displacements of Hf ions near the vacancy site by 4% and 8% of bulk separation distance for V_O^- and V_O^{2-}, respectively. The polarization of the lattice creates a potential well for the electrons, i.e., these localized states are polaronic in nature.

In order to rationalize this difference between HfO_2 and $LaAlO_3$, the following can be considered. In HfO_2, the oxygen vacancy is surrounded by four Hf^{4+} ions. The electrons in the negatively charged vacancy can be attributed to the Hf atomic d orbitals, which contribute to the bottom of the conduction band but, due to the vacancy-induced atom displacements, form localized gap states. Similarly, in $LaAlO_3$, the La d orbitals form the bottom of the conduction band. However, their displacement pattern near an oxygen vacancy is very different from that of Hf in HfO_2. In particular, each Hf^{4+} in HfO_2 is coordinated by eight O^{2-} ions, which can be considered as vertices of a distorted cube; in fact, HfO_2 adopts a monoclinic structure at low temperatures. Once an oxygen vacancy is formed, the Hf coordination number reduces to seven and an already low-symmetry potential energy surface becomes even more distorted, which makes large displacements of Hf atoms possible. This effect is assisted by the fact that formation of an oxygen vacancy in HfO_2, as well as in ZrO_2, induces a significant charge redistribution at the vacancy site [57,58].

In contrast, La^{3+} ion in LAO is confined by 12 O^{2-} ions and eight Al^{3+} ions, which create a symmetric, compact and rigid coordination shell. The formation of a neutral vacancy does not change the character of the charge distribution and, while it affects the symmetry and rigidity of the La environment, the effect is not strong enough to promote significant displacements of La^{3+} from its ideal lattice site. Hence the perturbation exerted on the electronic states at the bottom of the conduction band is not significant enough to induce localization of these states at the vacancy site and subsequent formation of V_O^-.

B. Defect properties

1. Optical absorption spectra

Optical absorption spectra for V_O^0 and V_O^+ have been calculated using the embedded cluster method and TDDFT, as implemented in GAUSSIAN09 [46]. The natures of the transition states and the orbitals have also been identified. The relative intensities of the peaks are determined by the oscillator strengths of the transitions, the lines are then broadened using a Gaussian function with a full width at half maxima of 0.2 eV. TDDFT calculations of transitions in the V_O^{2+} case did not demonstrate any subband-gap excitations with nonzero oscillator strengths, and as such absorption spectra are not shown.

The vacancies do not perturb the valence-band states as strongly as they do the conduction-band states. Hence, the VBM states remain delocalized and the transitions between them and the localized vacancy states have low intensities. It is also evident that the transitions from the O p orbitals at the top of the valence band to the vacancy state are prohibited by symmetry considerations.

The optical absorption spectra calculated for the neutral oxygen vacancies in the cubic and rhombohedral phases are shown in Fig. 7. Each spectrum is composed of several absorption peaks corresponding to transitions from the doubly occupied vacancy state [shown in Fig. 5(b)] to semilocalized states in the conduction band consisting primarily of La d orbitals. The spectrum for the rhombohedral lattice has a larger number of nondegenerate excited states, as expected for the lower-symmetry system. This spectrum is also shifted to the higher absorption energies by ~ 0.2 eV. We attribute this shift to the increased splitting of the e_g and t_{2g} manifold of the La d states caused by the lattice distortions, which shifts the e_g states, forming the bottom of the conduction band, up and increases the band gap (see Figs. 3 and 4). In order to ensure that the composition of the molecular orbitals obtained in the cluster calculations is not affected by the finite size of the quantum region, they were compared to the molecular orbitals obtained in the periodic method calculations and were found to be in good agreement.

As discussed above, the projected density of states (PDOS) of bulk LAO, calculated using the periodic method, shows that the bottom of the conduction band of cubic LAO is composed of e_g states, with equal contributions from the d_{z^2} and $d_{x^2-y^2}$ atomic orbitals, which are degenerate (see Fig. 4). The t_{2g} states are ~ 2.5 eV higher in energy than the e_g states. This is consistent with the crystal field splitting for a 12-coordinated La site, where the 12 nearest-neighbor O^{2-} ions are located along the t_{2g} lobes. The bottom of the conduction band of rhombohedral LAO is also composed of e_g-like states, though in this case the e_g-like states lie 0.2 eV higher in energy and there is a small splitting between the d_{z^2} and $d_{x^2-y^2}$ atomic orbitals. This is due to the difference in crystal field: the
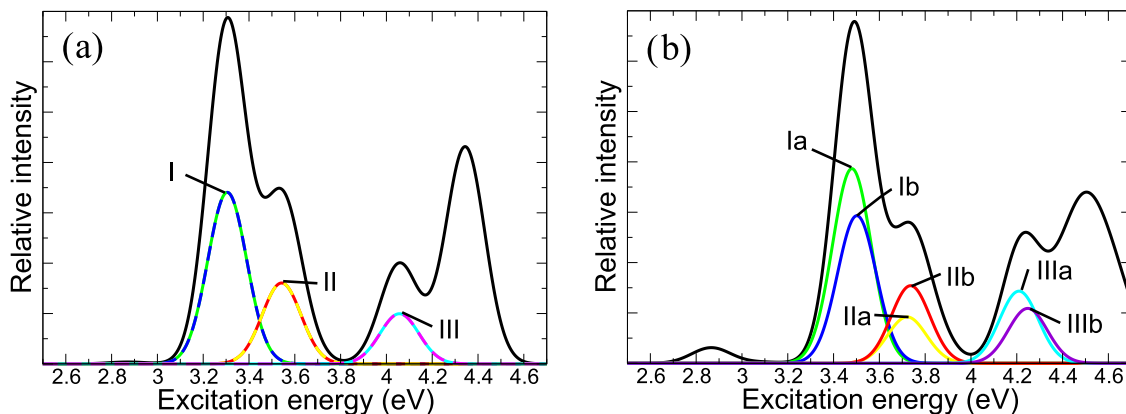
FIG. 7. The calculated absorption spectra for V_O^0 in the cubic (a) and rhombohedral (b) phases. The transitions have been broadened using Gaussian functions with a FWHM of 0.2 eV. The black lines show the total spectra, while the colored lines show the contributions due to the individual transition types. Dashed lines are used for visibility of degenerate transitions. All labels are defined in Fig. 3. The label I refers to the first, or lowest-energy transition in the cubic system, Ia and Ib refer to the two lowest energy transitions of the rhombohedral system, which unlike the cubic system are nondegenerate. This is repeated for the second (II) and third (III) transitions.

rhombohedral system can be produced by a slight distortion of the cubic lattice along with rotations of the oxygen octahedra. There is still a significant splitting between the e_g and t_{2g} states as the local environment of the La ions is similar between the cubic and rhombohedral cases. The rotation of the oxygen octahedra has a larger effect on the energies of the t_{2g} states, as the lobes of these orbitals no longer point directly towards the O sites, which causes the energies of the d_{xy}, d_{xz}, and d_{yz} orbitals to split.

The inclusion of the neutral vacancy perturbs certain states within the conduction band and, though the e_g-t_{2g} splitting remains dominant, there is some mixing of the states. In the cubic system, a contribution from the d_{xy} orbital to some states at the bottom of the conduction band ($\sim$ 7.2 eV) is observed. These states are localized in the vicinity of the vacancy, as shown in Fig. 8. The point symmetry of the defect is D_{4h}, with the irreducible symmetry of the vacancy state orbital being A_{1g} in character. This means the only symmetry-allowed dipole transitions are to states with an irreducible representation of E_u or A_{2u}. Where the perturbation of the states in the conduction band is small, the molecular orbitals display gerade

symmetry (see Fig. 8) and transitions are forbidden to these levels, resulting in the gaps in the absorption spectra.

The lowest energy absorption peak at 3.3 eV (transition I) in the cubic phase consists of two transitions to states where the biggest part of the wave function is composed of the d orbitals of the nearest-neighbor La ions to the vacancy [see Fig. 8(a)]. These orbitals display E_u symmetry and are therefore dipole operator allowed transitions. The second peak (transition II) with excitation energies of 3.5 eV involves states with a significantly smaller contribution from the d_{xy} orbital and are subsequently lower in intensity. The third set of peaks (transition III) with the onset at 4.06 eV involves more delocalized states with stronger contributions from the next-nearest-neighbor La ions.

In rhombohedral LAO, due to the lower symmetry of the defect site, the transition of type I splits into types Ia and Ib, as the unoccupied one-electron states involved in these transitions are no longer degenerate. However, as the perturbation to the local environment of the vacancy is small, the overall character of the absorption spectra remains the same, with the addition of some low intensity transitions to states that are
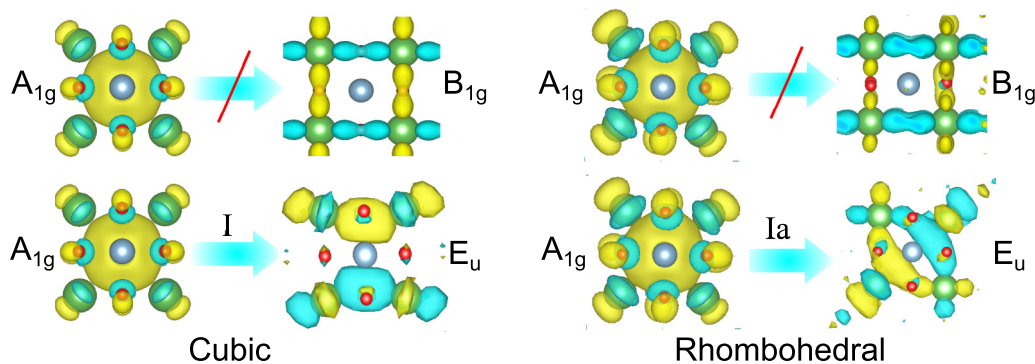

FIG. 8. The molecular orbitals involved in optical transitions from the vacancy state to states in the conduction band of cubic (left) and rhombohedral (right) LAO. The same molecular orbital of the vacancy can be seen in Fig. 5(b), here the vacancy lies behind the Al as viewed along the 001 crystal axis. The D_{4h} point symmetry of the defect can clearly be seen. The symmetry forbidden transitions (top) are to unperturbed e_g states at the bottom of the conduction band. The highest intensity transitions (bottom), I for cubic and Ia for rhombohedral, are allowed dipole transitions from an A_{1g} to an E_u state.
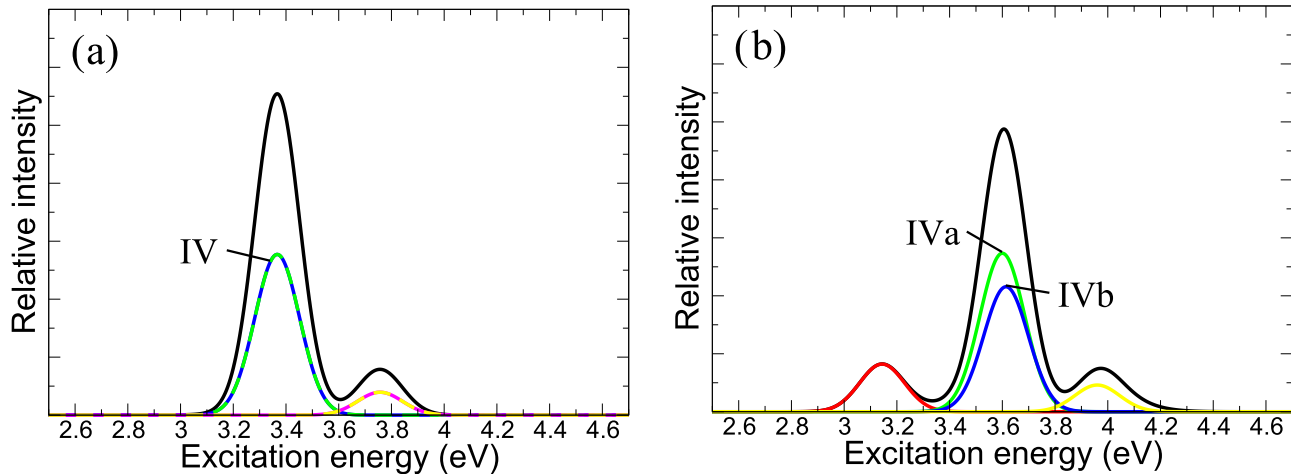
FIG. 9. The TDDFT calculated absorption spectra for V_O^+ in both the (a) cubic and (b) rhombohedral phases. The transitions have been widened using Gaussian functions with a FWHM of 0.2 eV.

no longer strictly symmetry forbidden. The same applies to the transitions of types II and III. The increased splitting of the individual t_{2g} states (d_{xy}, d_{xz} and d_{yz}) can be seen by the increased splitting of the transitions II and III compared to I.

The main absorption peak of the rhombohedral LAO at 3.5 eV (the peak extends from 3.2–4.0 eV) agrees well with the results of Kawabe *et al.* [26] who observe an absorption peak at 3.5–4.1 eV that is suppressed after oxidation of the sample, which they suggest is due to oxygen deficiency.

The absorption spectra for V_O^+ differ from those of the neutral vacancy. In particular, they exhibit a single large peak and no significant second peak at higher energy (see Fig. 9). Similarly to the case of the neutral vacancy, the energy of the maximum of the absorption peak obtained for the rhombohedral lattice is ~ 0.2 eV higher than that for the cubic lattice. The transitions from the valence band to the unoccupied V_O^+ level in the band gap are calculated to have a negligible oscillator strength, as such we only see transitions from the occupied vacancy level to the conduction band in the absorption spectra. This is most likely because, like in the V_O^{2+} case, the O p states that compose the valence band are not significantly perturbed by the defect to create resonant states with appropriate symmetry. The states involved in transition IV (see Fig. 9) are similar to those involved in transition I in the neutral case. This is expected as the V_O^+ defect shares the same point symmetry as V_O^0. The rhombohedral system demonstrates a nonzero transition below transition IV not seen in the cubic case. In the rhombohedral case, there is weak localization of the molecular orbital composed of a mixing of the t_{2g} states with the predominantly e_g states at the bottom of the conduction band. In the cubic case, both of these orbitals are delocalized pure e_g states and so there are no transitions to these states.

2. The g tensor and hyperfine splittings of V_O^+

Electron spin resonance (ESR) studies can allow measurements of the V_O^+ defect in LAO. Indeed, ESR studies of LAO [28,29] have attributed certain signals in their measured spectra to this defect. In order to confirm the prediction that these signals are due to the V_O^+ defect, the g tensor and hyperfine

values of the defect can be calculated and compared to the experimental values.

The g-tensor components for the $+1$ charged oxygen vacancy, calculated using Gaussian 09 [46] and the embedded cluster method, are shown in Table II. The calculated hyperfine splittings show the main contribution to the ESR signal comes from the nearest neighbor Al ions. This is most likely because the defect orbital is mostly composed of the p orbitals of these Al ions. The calculated value of the splitting is small at 0.53–0.69 mT, dependent on the local structure. The contributions of the nearest-neighbor O ions are smaller at approximately 0.1 mT and only apply if grown in ^{18}O as naturally abundant ^{16}O has zero nuclear spin. The contributions of even the nearest neighbor La are negligible.

The calculated g values agree closely with the ESR results of Yamasaka *et al.* [28] and Singh *et al.* [29]. The former work assigns a broad ESR signal at approximately 328 mT to the $+1$

TABLE I. Interatomic distances (in angstroms) and magnitude of vacancy-induced displacements (as a percentage change in interatomic distance from bulk) in LAO. Negative and positive values of the displacements indicate relaxation towards and away from the vacancy site, respectively. A diagram defining the nearest-neighbor distances is shown in Fig. 5(a).

		Embedded cluster		Periodic	
		$Pm\bar{3}m$	$R\bar{3}c$	$Pm\bar{3}m$	$R\bar{3}c$
Interatomic nearest-neighbor distances (Å)	Al-Al	3.82	3.79	3.79	3.79
	La-La	5.42	5.38	5.36	5.36
	O-O	5.40	5.35–5.37	5.36	5.36
	V_O^0 Al-Al	-2.5	-2.0	0.2	-0.0
	La-La	0.7	0.2	-0.2	-0.8
Maximum displacements from perfect lattice (%)	O-O	-0.8	-0.7	-0.2	-0.9
	V_O^{1+} Al-Al	2.7	2.8	4.5	5.4
	La-La	2.8	2.4	1.9	1.7
	O-O	-2.7	-2.3	-2.6	-2.8
	V_O^{2+} Al-Al	7.9	7.4	8.0	9.5
	La-La	4.3	4.5	4.2	4.2
	O-O	-6.0	-6.5	-6.1	-6.2

TABLE II. The calculated g-tensor values of V_O^+ for both the cubic and rhombohedral LAO structures. The $Al^{3+}-V_O^+-Al^{3+}$ complex is oriented along the x axis of the cubic cell.

	Calculated g tensor		
	g_{xx}	g_{yy}	g_{zz}
$Pm\bar{3}m$	1.999338	2.005083	2.005083
$R\bar{3}c$	2.004025	2.000608	2.003056

charged oxygen vacancy in LAO. We can use their reported X-band frequency of 9.2 GHz to calculate the corresponding g value to be 2.004022, which is in good agreement with the calculated values. The width of the signal reported by Yamasaka *et al.* [28] is approximately 4.0 mT, which can be explained by the calculated hyperfine splittings. Al has a nuclear spin of 5/3, which means the hyperfine interaction leads to six peaks split by approximately 0.6 mT, this would lead to a total broadening of at least 3.0 mT, assuming that the broadening of each line was large enough that the individual lines could not be resolved. This also agrees well with the results of Singh *et al.* [29] who measured the line width of the V_O^+ signal to be 2.9 mT. They also suggest hyperfine interaction with the nearest neighbor cations are the main contribution to the linewidth, in agreement with our calculations.

Also of interest are the absorption spectra measured by Yamasaka *et al.* [28]. The ESR signal for the charged vacancy only appears as the number of incident photons (with photon energy peak at 5.03 eV) increases on the LAO sample while it is under UV irradiation. This corresponds to an increase in the absorption coefficient at approximately 3.3 and 4.0 eV. These energies lie close to the transition energies for the neutral and charged oxygen vacancies calculated using TDDFT and could well explain the increase in both these signals.

IV. CONCLUSION

Our calculations provide the absorption spectra and ESR signatures for oxygen vacancies in LAO that can be used to identify these defects experimentally. The electronic and geometric structure of the neutral and charged oxygen vacancies in the band gap of LAO were calculated using periodic and embedded cluster methods and hybrid density functionals. The optical absorption spectra of V_O^0 and V_O^+ were calculated using TDDFT. The optical absorption spectra of V_O^+ in rhombohedral LAO, which has an intensity maximum at 3.5 eV and a peak that extends from 3.2 eV to 4.0 eV, agrees well with the experimental results of Kawabe *et al.* [26] who see an absorption tail at 3.5–4.1 eV that they attribute to oxygen deficiency. The optical absorption spectrum for the neutral vacancy in cubic LAO, which shows an intensity maximum at 3.3 eV, has also been calculated. Both the cubic and rhombohedral absorption spectra exhibit a second absorption peak at 4.0 and 4.2 eV, respectively. The V_O^+ only exhibits one peak at 3.4 eV (cubic) and 3.6 eV (rhombohedral) which potentially allows identification of the two different charge states of the defect.

Also presented are the calculated ESR parameters of V_O^+ in LAO. The isotropic g value was calculated to be 2.004026, and, due to hyperfine splitting of the nearest neighbor Al ions to the vacancy, a signal broadening of 3.0 mT is predicted. These calculations agree well with reported ESR experimental results. [28,29]. The calculated absorption spectra of the V_O^+ can also be used to explain the absorption peaks observed by Yamasaka *et al.* [28] that appear with increased ESR signal assigned to V_O^+.

[1] N. C. Bristowe, P. Ghosez, P. B. Littlewood, and E. Artacho, J. Phys.: Condens. Matter **26**, 143201 (2014).

[2] S. Gariglio, A. Fête, and J.-M. Triscone, J. Phys.: Condens. Matter **27**, 283201 (2015).

[3] S.-G. Lim, S. Kriventsov, T. N. Jackson, J. H. Haeni, D. G. Schlom, A. M. Balbashov, R. Uecker, P. Reiche, J. L. Freeouf, and G. Lucovsky, J. Appl. Phys. **91**, 4500 (2002).

[4] E. Cicerrella, J. L. Freeouf, L. F. Edge, D. G. Schlom, T. Heeg, J. Schubert, and S. A. Chambers, J. Vac. Sci. Technol. A **23**, 1676 (2005).

[5] M. Suzuki, T. Yamaguchi, N. Fukushima, and M. Koyama, J. Appl. Phys. **103**, 034118 (2008).

[6] Y. Y. Mi, Z. Yu, S. J. Wang, P. C. Lim, Y. L. Foo, A. C. H. Huan, and C. K. Ong, Appl. Phys. Lett. **90**, 181925 (2007).

[7] A. Ohtomo and H. Y. Hwang, Nature (London) **427**, 423 (2004).

[8] N. Nakagawa, H. Y. Hwang, and D. A. Muller, Nat. Mater. **5**, 204 (2006).

[9] Z. S. Popovic, S. Satpathy, and R. M. Martin, Phys. Rev. Lett. **101**, 256801 (2008).

[10] R. Pentcheva and W. E. Pickett, Phys. Rev. B **78**, 205106 (2008).

[11] N. C. Bristowe, P. B. Littlewood, and E. Artacho, Phys. Rev. B **83**, 205405 (2011).

[12] W. Siemons, G. Koster, H. Yamamoto, W. A. Harrison, G. Lucovsky, T. H. Geballe, D. H. A. Blank, and M. R. Beasley, Phys. Rev. Lett. **98**, 196802 (2007).

[13] P. R. Willmott *et al.*, Phys. Rev. Lett. **99**, 155502 (2007).

[14] S. A. Chambers *et al.*, Surf. Sci. Reports **65**, 317 (2010).

[15] L. Qiao, T. C. Droubay, V. Shutthanandan, Z. Zhu, P. V. Sushko, and S. A. Chambers, J. Phys.: Condens. Matter **22**, 312201 (2010).

[16] L. Qiao, T. C. Droubay, T. C. Kaspar, P. V. Sushko, and S. A. Chambers, Surf. Sci. **605**, 1381 (2011).

[17] M. P. Warusawithana *et al.*, Nat. Commun. **4**, 2351 (2013).

[18] Z. Q. Liu, L. Sun, Z. Huang, C. J. Li, S. W. Zeng, K. Han, W. M. Lü, and T. Venkatesan, J. Appl. Phys. **115**, 054303 (2014).

[19] L. Yu and A. Zunger, Nat. Commun. **5**, 5118 (2014).

[20] M. Huijben *et al.*, Adv. Funct. Mater. **23**, 5240 (2013).

[21] C. J. Howard, B. J. Kennedy, and B. C. Chakoumakos, J. Phys.: Condens. Matter **12**, 349 (2000).

[22] J. Wang, N. Ishizawa, and X. Ye, J. Alloys Compd. **594**, 23 (2014).

[23] R. L. Johnson-Wilke *et al.*, Phys. Rev. B **88**, 174101 (2013).

[24] J. Park, Y.-A. Soh, G. Aeppli, A. David, W. Lin, and T. Wu, Appl. Phys. Lett. **104**, 081604 (2014).

[25] A. N. Meza-Rocha, E. Zaleta-Alejandre, J. G. Cabanas-Moreno, S. Gallardo-Hernandez, Z. Rivera-Alvarez, M. Aguilar-Frutis, and C. Falcony, ECS J. Solid State Sci. Technol. **3**, N1 (2013).

[26] Y. Kawabe, A. Yamanaka, E. Hanamura, T. Kimura, Y. Takiguchi, H. Kan, and Y. Tokura, J. Appl. Phys. **88**, 1175 (2000).

[27] J. Q. Chen *et al.*, Appl. Phys. Lett. **98**, 041904 (2011).

[28] D. Yamasaka, K. Tamagawa, and Y. Ohki, J. Appl. Phys. **110**, 074103 (2011).

[29] V. Singh, S. Watanabe, T. G. Rao, J. Chubaci, and H.-Y. Kwak, Solid State Sciences **13**, 66 (2011).

[30] K. Xiong, J. Robertson, and S. J. Clark, Appl. Phys. Lett. **89**, 022907 (2006).

[31] X. Luo, B. Wang, and Y. Zheng, Phys. Rev. B **80**, 104115 (2009).

[32] C. Mitra, C. Lin, J. Robertson, and A. A. Demkov, Phys. Rev. B **86**, 155105 (2012).

[33] F. El-Mellouhi, E. N. Brothers, M. J. Lucero, and G. E. Scuseria, Phys. Rev. B **88**, 214102 (2013).

[34] M. Choi, A. Janotti, and C. G. Van de Walle, Phys. Rev. B **88**, 214117 (2013).

[35] J. Heyd, G. E. Scuseria, and M. Ernzerhof, J. Chem. Phys. **118**, 8207 (2003).

[36] E. Runge and E. K. U. Gross, Phys. Rev. Lett. **52**, 997 (1984).

[37] M. A. L. Marques and E. K. U. Gross, Ann. Rev. Phys. Chem. **55**, 427 (2004).

[38] D. Muñoz Ramo, P. V. Sushko, J. L. Gavartin, and A. L. Shluger, Phys. Rev. B **78**, 235432 (2008).

[39] I. V. Abarenkov, Phys. Rev. B **76**, 165127 (2007).

[40] P. V. Sushko and I. V. Abarenkov, J. Chem. Theory Comput. **6**, 1323 (2010).

[41] R. Krishnan, J. S. Binkley, R. Seeger, and J. A. Pople, J. Chem. Phys. **72**, 650 (1980).

[42] A. D. McLean and G. S. Chandler, J. Chem. Phys. **72**, 5639 (1980).

[43] L. E. Roy, P. J. Hay, and R. L. Martin, J. Chem. Theory Comput. **4**, 1029 (2008).

[44] P. J. Hay and W. R. Wadt, J. Chem. Phys. **82**, 299 (1985).

[45] K. L. Schuchardt, B. T. Didier, T. Elsethagen, L. Sun, V. Gurumoorthi, J. Chase, J. Li, and T. L. Windus, J. Chem. Inf. Model. **47**, 1045 (2007).

[46] M. J. Frisch *et al.*, GAUSSIAN09 revision a.02, Gaussian Inc. Wallingford CT 2009.

[47] J. Heyd, G. E. Scuseria, and M. Ernzerhof, J. Chem. Phys. **124**, 219906 (2006).

[48] J. VandeVondele, M. Krack, F. Mohamed, M. Parrinello, T. Chassaing, and J. Hutter, Comput. Phys. Commun. **167**, 103 (2005).

[49] M. Guidon, J. Hutter, and J. VandeVondele, J. Chem.l Theor. Comp. **5**, 3010 (2009).

[50] J. VandeVondele and J. Hutter, J. Chem. Phys. **127**, 114105 (2007).

[51] S. Goedecker, M. Teter, and J. Hutter, Phys. Rev. B **54**, 1703 (1996).

[52] C. Hartwigsen, S. Goedecker, and J. Hutter, Phys. Rev. B **58**, 3641 (1998).

[53] A. Popov, E. Kotomin, and J. Maier, Nucl. Instrum. Methods Phys. Res., Sect. B **268**, 3084 (2010).

[54] S. Lany and A. Zunger, Phys. Rev. B **78**, 235104 (2008).

[55] Y. Zhukovskii, E. Kotomin, S. Piskunov, and D. Ellis, Solid State Commun. **149**, 1359 (2009).

[56] A. Stoneham, J. Gavartin, A. Shluger, A. Kimmel, D. Muñoz Ramo, H. M. Rønnow, G. Aeppli, and C. Renner, J. Phys.: Condens. Matter **19**, 255208 (2007).

[57] A. S. Foster, F. Lopez Gejo, A. L. Shluger, and R. M. Nieminen, Phys. Rev. B **65**, 174117 (2002).

[58] A. S. Foster, V. B. Sulimov, F. Lopez Gejo, A. L. Shluger, and R. M. Nieminen, Phys. Rev. B **64**, 224108 (2001).